Tailoring the Electrochemical Performance of SnO_2-Based Anodes for Li-Ion Batteries: Effect of Morphology and Composite Matrix

Antunes Staffolani, Leonardo Sbrascini, Gilberto Carbonari, Fabio Maroni, Luca Minnetti, Luca Bottoni, and Francesco Nobili*

Three different composite anodes, based on SnO_2, are investigated as potential anode materials for lithium-ion batteries. Three different strategies have been employed to stabilize SnO_2 upon cycling, i.e., i) use of an inorganic matrix (TiO_2), ii) use of an amorphous carbon matrix, and iii) use of SnO_2 with a tailored morphology (nanorod) and a carbon coating. Specific capacities, ranging from 700 up to 1000 mAh g^{-1}, are obtained during galvanostatic cycles with high-capacity retentions. Furthermore, this work sheds light on the interfacial and transport properties of such electrode materials, given by cyclic voltammetry at different scan rates, galvanostatic intermittent titration technique, and electrochemical impedance spectroscopy.

1. Introduction

Nowadays, Li-ion batteries are the devices of choice for energy storage applications; however, further developments are still needed, especially when considering applications such as (hybrid-) electric vehicles.[1] The performance of these devices are intrinsically dependent on the materials used in the main components, i.e., anode, cathode, and electrolyte. In this regard, anode(cathode) materials having high specific capacities and low(high) working voltages are needed to meet the required energy density in such applications. Furthermore, when considering large markets such as transport electrification, and stationary storage particular attention must be paid to the sustainability and availability of the materials employed.[2] On the positive electrode side, several materials have already been successfully commercialized such as layered oxides with low Co content ($LiNi_{1\text{-}x\text{-}y}Mn_xCo_yO_2$ and $LiNi_{0.8}Co_{0.15}Al_{0.05}O_2$),[3] and olivine phosphates ($LiFePO_4$), while other materials such as high voltage spinel[4,5] ($LiNi_{0.5}Mn_{1.5}O_4$) and multi metal olivine phosphates ($LiM_xFe_{1\text{-}x}PO_4$) are in the development stage.[6,7] On the other hand, the focus on negative electrode materials is rather restricted to the commercially widespread graphite, and next-generation anode materials, i.e., silicon, and silicon oxides.[8,9] However, all of them are included in the current critical raw materials list of the European Union[10] and, thus, their supply, production, and application in the European market are hindered. As an alternative, a recent class of materials called conversion-alloying materials (CAMs), which provide energy and Li storage via conversion and alloying reactions, were proposed. These materials are commonly oxides or sulfides of metal elements which are reduced upon lithiation to the metal nanoparticles and lithium oxide or sulfide (conversion reaction); consequently, the formed metal nanoparticles react with Li via an alloying reaction. Metals like Sn, Sb, Zn, Ge, etc. can form oxides and sulfides which work according to a conversion-alloying mechanism and have been already intensively studied as candidate anode materials.[11,12] Among them, SnO_2 has attracted particular interest thanks to its high specific capacity of 1494 mAh g^{-1}.[13] However, like all CAMs, it suffers from a drastic capacity fading due both to its structural rearrangement (given by the conversion reaction) and volume expansion upon lithiation (given by the

---

A. Staffolani, L. Sbrascini, G. Carbonari, F. Maroni[+], L. Minnetti,
L. Bottoni, F. Nobili
School of Science and Technology – Chemistry Division
University of Camerino
Via Madonna delle Carceri, Camerino I-62032, Italy
E-mail: antunes.staffolani@unibo.it

A. Staffolani
Department of Chemistry "Giacomo Ciamician"
University of Bologna
Via Piero Gobetti 85, Bologna 40129, Italy

A. Staffolani
ENERCube Lab
Centro Ricerche Energia
Ambiente e Mare
Centro Interdipartimentale per la Ricerca Industriale Fonti Rinnovabili
Ambiente
Mare ed Energia (CIRI-FRAME)—Alma Mater Studiorum University of
Bologna
Viale Ciro Menotti, 48, Marina di Ravenna 48122, Italy

F. Nobili
GISEL - Centro di Riferimento Nazionale per i Sistemi di Accumulo Elettrochimico di Energia
INSTM
Via G. Giusti 9, Firenze I-50121, Italy

The ORCID identification number(s) for the author(s) of this article can be found under https://doi.org/10.1002/admt.202402058

[+]Present address: Zentrum für Sonnenenergie- und Wasserstoff-Forschung Baden-Württemberg, 89081 Ulm, Germany

DOI: 10.1002/admt.202402058

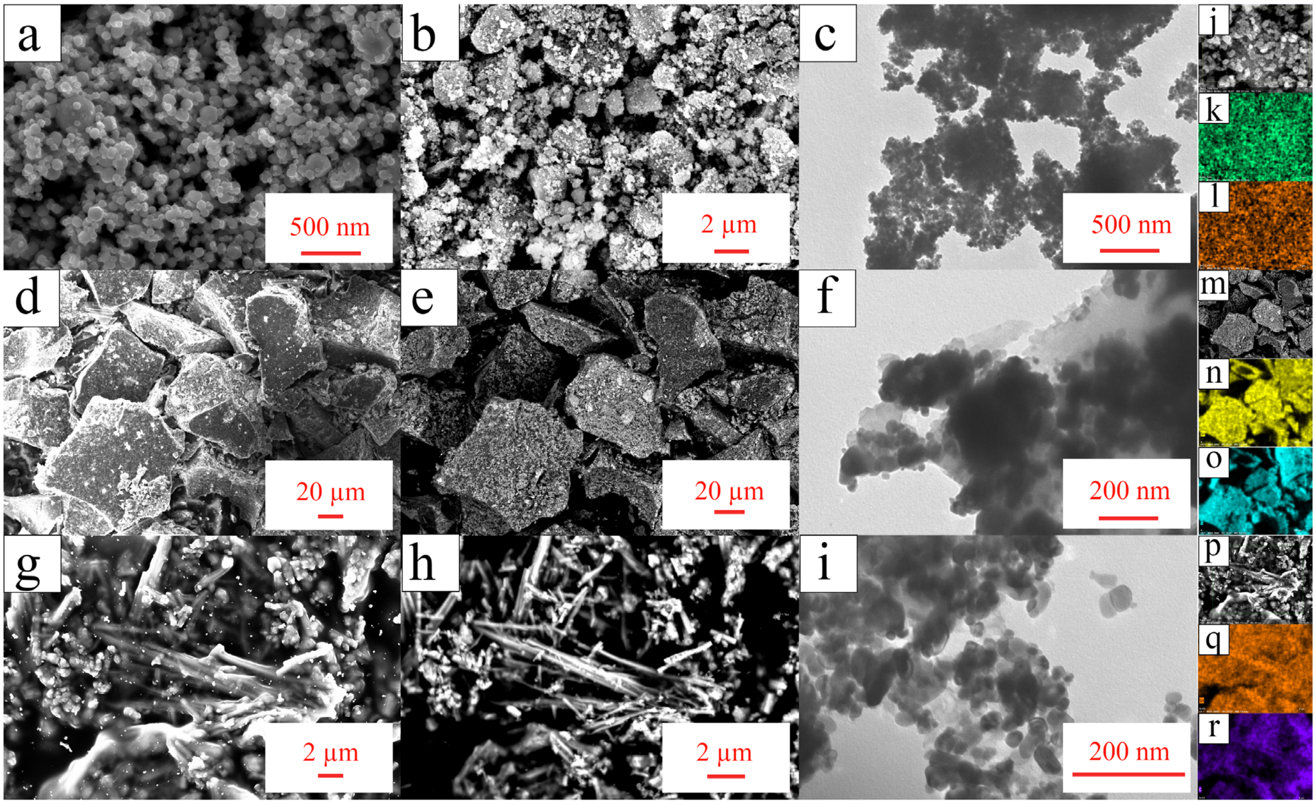

Figure 1. a) SEM micrographs of a bare commercial SnO_2 nanopowder. b,c) SEM and TEM micrographs of SnO_2TiO_2 acquired at the magnification levels 10 and 25 kX, respectively. d) Secondary electrons micrograph of SnO_2/C acquired at the magnification level 500 X. e) Backscattered electrons micrograph of SnO_2/C acquired at the magnification level 500 X. f) TEM micrograph of SnO_2/C acquired at the magnification level 50 kX. g) Secondary electrons micrograph of C/SnO_2NR acquired at the magnification level 500 X. h) Backscattered electrons micrograph of C/SnO_2NR acquired at the magnification level 500 X. i) TEM micrograph of C/SnO_2NR acquired at the magnification level 100 kX. EDX elemental map of j–l) SnO_2TiO_2 (green = Sn, orange = Ti), m–o) SnO_2/C (yellow = Sn, azure = C), and p–r) C/SnO_2NR (q = Sn, purple = C).

alloying reaction). Several strategies have been employed in literature such as i) metal-doping with elements which do not undergo the alloying reaction[14–16] (for instance Co, Mn, Ni, etc.), ii) preparation of composites with either carbon matrices[17,18] and/or other inorganic compounds,[19,20] and iii) synthesis of nanostructured materials such as nanoparticle,[18,21] nanowires,[22–24] nanotubes,[24,25] and hollow nanostructures[26] able to "accommodate" the volume expansion occurring during the alloying reaction. Other promising approaches include the encapsulation of the metal oxide in a carbon matrix as reported in ref. [27], and hybrid structures with other alloying materials such as Silicon or Antimony.[28,29]

In this paper, a comparison study between three different strategies employed for the stabilization of SnO_2 as anode material is reported. The different approaches are: i) use of an active inorganic matrix made of anatase TiO_2 as a buffering agent (SnO_2/TiO_2), use of an active carbonaceous matrix (SnO_2/C), and use of nanostructured morphology (C/SnO_2 nanorods). The structure and morphology of the composites were assessed and compared by scanning electron microscopy (SEM), transmission electron microscopy (TEM), X-Ray Diffraction (XRD), and Raman spectroscopy. The carbon content was quantified by thermogravimetric analysis (TGA). The electrochemical performance, as well as the transport and interfacial properties of the materials, were assessed by galvanostatic cycling, cyclic voltammetry, rate capability, cyclic voltammetry at different scan rates, galvanostatic intermittent titration technique, and potentiostatic electrochemical impedance spectroscopy.

2. Results and Discussion

2.1. Structural and Morphological Characterization

In **Figure 1**, the TEM, SEM, as well as elemental mapping of the three studied composite anodes are reported. The bare SnO_2 nanopowder (Figure 1a) is composed of spherical particles with a diameter of ≈ 100 nm, as provided by the manufacturer. In the case of SnO_2/TiO_2 (Figure 1b,c), large particles made of the as-synthesized TiO_2 are visible and covered with SnO_2 particles. This feature is also confirmed in the SEM micrograph taken at higher magnification (Figure S1a, Supporting Information), in which the large aggregates are covered by spherical particles with diameter < 100nm. In the case of SnO_2/C (Figure 1d), the composite material is constituted by large porous particles of several micrometers. As shown in Figure S1b (Supporting Information), it is not possible to discern the distribution of the SnO_2 particles in the carbon matrix. However, by observing the sample with backscattered electrons (Figure 1e), the surface of these

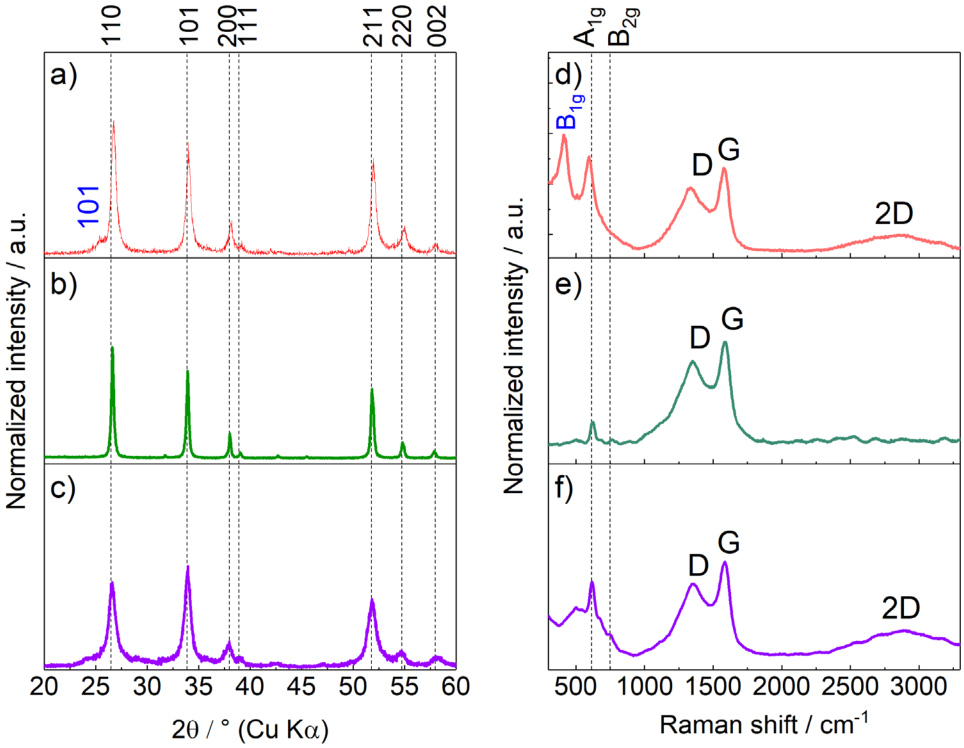

Figure 2. Diffraction patterns of a) SnO_2/TiO_2, b) SnO_2/C, and c) C/SnO_2NR. Raman spectra of d) SnO_2/TiO_2, e) SnO_2/C, and f) C/SnO_2NR.

particles appears porous and covered with light spots, indicating the presence of Sn. The TEM micrograph (Figure 1f) suggests an embedding of the SnO_2 particles into the hard carbon matrix. C/SnO_2NR is characterized by a rod-like morphology with uneven diameter (ranging from 0.5 µm up to 2 µm). At higher magnification levels (Figure S1c, Supporting Information) it is clearly depicted that the rods are made of assembled SnO_2 particles with Ø < 100 nm. On the TEM micrograph (Figure 1i) taken at high magnification (100 kX) two overlapped rods are shown, further confirming that they are made of assembled SnO_2 with Ø < 100 nm. The carbon coating was confirmed by comparing Figure 1g,h, which were acquired with secondary and backscattered electrons, respectively. In the micrograph acquired with secondary electrons, the rods are embedded in the carbon matrix and can be seen by a slight transparency. This feature was confirmed in the image acquired with the backscattered electrons in which the carbon matrix is not visible and, as expected, only the brighter response from SnO_2 can be detected. Elemental mapping given by EDX confirmed the uniform distribution of Sn and Ti in SnO_2/TiO_2 (Figure 1j–l), Sn and C in SnO_2/C (Figure 1m–o), and Sn and C in C/SnO_2NR (Figure 1p–r).

The carbon content was assessed by thermogravimetric analysis (Figure S2, Supporting Information). The weight losses due to the oxidation of C to CO_2 were 12.44%, 44.04%, and 11.64% for SnO_2/TiO_2, SnO_2/C, and C/SnO_2NR, respectively.

In **Figure 2** the experimental diffractograms as well as the experimental Raman spectra of the three studied composites are reported. In all three cases, the SnO_2 cassiterite phase (space group $P4_2/mnm$),[30] was confirmed by both diffraction patterns and the presence of the A_{1g} and B_{2g} bands, located at 623 and 766 cm^{-1}, in the Raman spectra.[31,32] Further Raman peaks related to SnO_2 are visible in the samples SnO_2/C and C/SnO_2NR, i.e., 500, and 766 cm^{-1}, ascribed to the A_{2u} ν(TO), and B_{2g} modes, respectively, and are reported in Figure S3 (Supporting Information). In the case of SnO_2/TiO_2, additional features were detected in both XRD and Raman spectrum, i.e., a peak at 25.5 °, and a signal at 423 cm^{-1}. The former was indexed to the 101 sets of planes of anatase TiO_2,[33] while the latter was assigned to the B_{1g} mode of anatase TiO_2 (RRUFF database, RRUFF-ID R060277.3).

The D and G bands of each spectra were fit with a Gaussian-Lorentzian function[34] (**Figure 3**). The two most intensive peaks are the D_1 and G bands, which can be assigned to the disordered sp^3 C atoms or defective graphitic structures (A_{1g} vibration of C_6 rings), and in-plane stretching motion between sp^2 carbon atoms (E_{2g} vibration mode), respectively. The D_3 band can be assigned to the lattice vibration similarly to the G-band, while the D_2 can be assigned to oxygen-containing moieties. At last, D_4 is assigned to the sp^2–sp^3 bonds at the edge of the graphite crystallite.[34] From the fit result, the I_D/I_G ratio, as well as the domain size of the defective structure (L_a, Equation (1)).

$$L_a\,(nm) = 2.4 \cdot 10^{-10}\,\lambda_{nm}^4\,\frac{I_D}{I_G} \qquad (1)$$

where λ_{nm} is the wavelength of the excitation source in the Raman spectrometer (532 nm). The calculated I_D/I_G ratios for SnO_2/TiO_2, SnO_2/C, and C/SnO_2NR were 1.95, 1.87, and 2.31, respectively. From these results, it was possible to calculate a domain size L_a of 37.48 nm, 35.95 nm, and 44.41 nm for

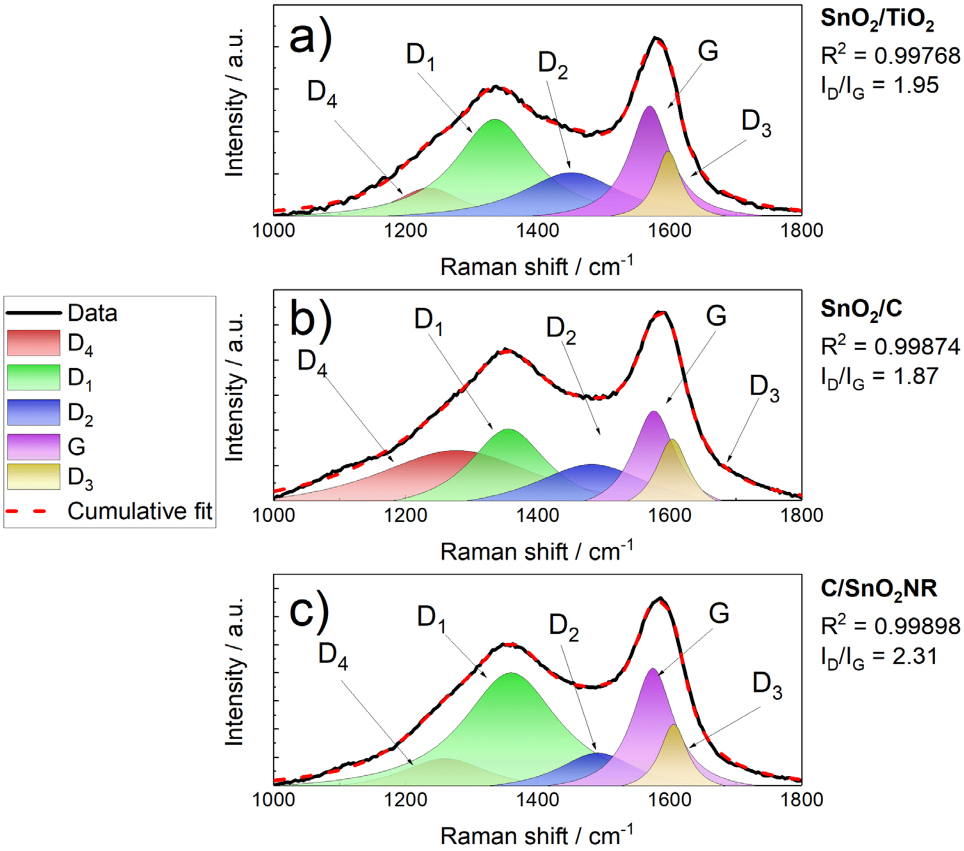

Figure 3. Fitted D and G bands in the Raman spectra of a) SnO_2/TiO_2, b) SnO_2/C, and C/SnO_2NR with their respective R^2 and I_{D1}/I_G ratios. D_4 = red, D_1 = green, D_2 = blue, G = purple, and D_3 = yellow.

SnO_2/TiO_2, SnO_2/C, and C/SnO_2NR, respectively. The calculated I_D/I_G ratios and L_a are summarized in **Table 1**.

2.2. Electrochemical Characterization

In **Figure 4a–c** the 1st and 2nd cycles of cyclic voltammetry of SnO_2/TiO_2, SnO_2/C, and C/SnO_2NR are reported. In all three cases, a similar electrochemical behavior was observed, with a sharp peak at E = 0.8 V (A) in the first cycle and a larger peak at E = 0.2 V (B). Two more peaks were detected only in the case of SnO_2/TiO_2 at E = 1.71 V (T) and E = 1.09 V (**V**) due to the lithiation of TiO_2 into Li_xTiO_2[35] and the polymerization of the VC additive at the electrode surface giving a stable film made of poly alkyl Li-carbonate species.[36]

Table 1. Summary of the calculated I_D/I_G ratios and domain size.

	I_D/I_G	L_a [nm]
SnO_2/TiO_2	1.95	37.48
SnO_2/C	1.87	35.95
C/SnO_2NR	2.31	44.41

The two peaks A and B can be assigned to the conversion reaction and alloying reaction, respectively, as described by the following equations Equations (2) and (3):[13,37]

$$\text{Conversion reaction } SnO_2 + 4e^- + 4Li^+ \rightarrow Sn + 2Li_2O \tag{2}$$

$$\text{Alloying reaction } Sn + 4.4Li^+ + 4.4e^- \leftrightarrow Li_{4.4}Sn \tag{3}$$

In the conversion reaction, the metal oxide is reduced with the formation of the corresponding metal nanoparticles (Sn) and a matrix of Li_2O.[13] Subsequently, in the alloying reaction, the formed Sn metal will form an alloy with Li. However, the conversion reaction is a partly irreversible reaction[13,37]; indeed, during the second cathodic scan only a broad and less intense peak can be observed. Furthermore, this behavior is confirmed by the two broad peaks observed during the anodic scan at E = 1.26 V (A') and E ≈ 1.91 V (A'') which can be assigned to the incomplete oxidation of Sn metal to its higher oxidation states.[13,37] This issue was attributed in literature to several reasons such as i) formation of large metal clusters upon the reduction reaction, which can hinder the kinetics of the oxidation reaction afterward, and ii) a larger energy barrier for the oxidation of Sn compared to other TMs.[13,38] Eventually, this will lead to the coarsening and the migration of the active material particles toward the electrode surface.

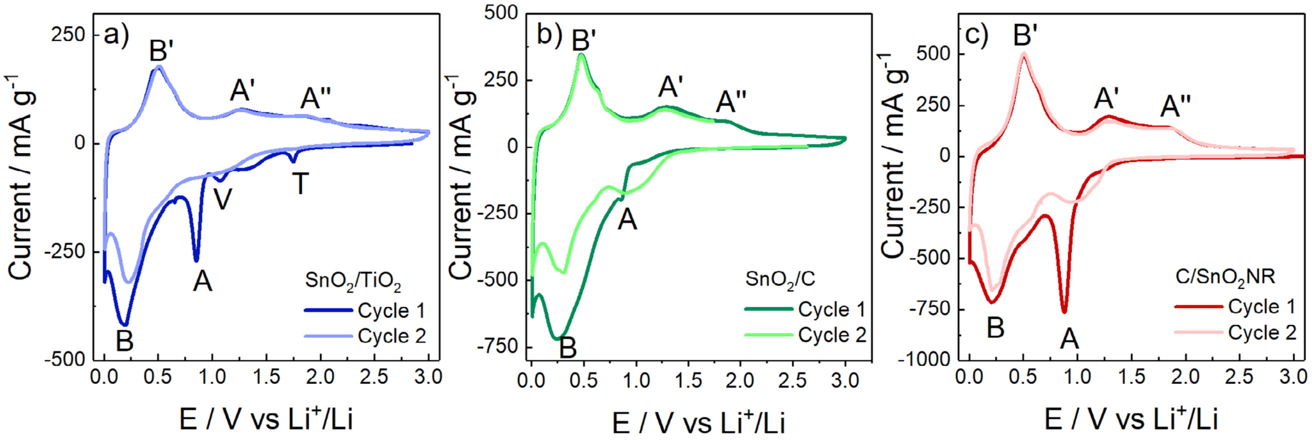

Figure 4. Cyclic voltammetry was acquired during the first and second cycles of a) SnO$_2$/TiO$_2$, b) SnO$_2$/C, and c) C/SnO$_2$NR. $\nu = 0.05$ mV s^{-1}, $0.010 < E < 3.000$ V versus Li$^+$/Li.

On the other hand, the alloying reaction is a reversible process. Indeed, a peak at E = 0.49 V (B) was observed during the anodic scan and was assigned to the extraction of Li$^+$ from the Li$_x$Sn alloy. In addition, during the first scan at E < 0.8 V the formation of the Solid Electrolyte Interphase (SEI) occurs,[39] which can be observed by the difference in intensity of the peak B between the first and second scan. SnO$_2$/C has shown slightly different redox behavior when compared with the other two composite anode materials, especially peak A due to the conversion reaction, which is visibly less intense. This phenomenon is assigned to the larger amount of carbon in SnO$_2$/C (44.04% as shown in Figure S2, Supporting Information) compared to the other composite anode materials. Indeed, in the same potential region of peak A, the intercalation of Li$^+$ ions into hard carbon also occurs,[40] which can explain the decrease of its intensity when compared with the other two composite anode materials. In addition, the SEI formation may be affected by the larger percentage of amorphous carbon.[39]

Preliminary galvanostatic cycles were performed by applying a CC-CV protocol, with a specific current $I_{Spec} = 1$ A g^{-1} and a constant voltage period at E = 0.010 V during lithiation until the current reached the value $I_{CV} = 0.1$ A g^{-1}.[35] The results are reported in **Figure 5**. In the case of SnO$_2$/TiO$_2$, in the first lithiation/delithiation, specific capacity values of 1763 and 1013 mAh g^{-1} were reached respectively, with an efficiency of 57%. The low coulombic efficiency in the first cycle clearly reflects the occurrence of the mentioned irreversible processes, i.e., i) SEI formation and ii) reduction of SnO$_2$ to Sn. After a slight decrease in the first few cycles, the material was able to deliver a stable specific capacity of ≈900 mAh g^{-1}.

In the case of SnO$_2$/C, a coulombic efficiency of 62% was observed, probably due to the lower amount of SnO$_2$ in the composite with respect to SnO$_2$/TiO$_2$ (56% versus 66% for SnO$_2$/C and SnO$_2$/TiO$_2$, respectively). However, the lower amount of SnO$_2$ also resulted in a lower specific capacity upon cycling with values of ≈800 mAh g^{-1}. In both SnO$_2$/TiO$_2$ and SnO$_2$/C, coulombic efficiencies > 100% were observed after 60 cycles which are due to the formation of dendrites at the counter electrode.[41]

In the last case (C/SnO$_2$NR), an initial coulombic efficiency of 65% was observed, even if this composite has the highest SnO$_2$ content among the three tested composite anodes. During the further cycles, a specific capacity of ≈1000 mAh g^{-1} was observed, with a decay in the last 20 cycles.

The results obtained by galvanostatic cycling are summarized in **Table 2**.

The galvanostatic E versus Q profiles extracted from the 1st and the 100th cycle are reported in Figure 5b,c. In the first lithiation of SnO$_2$/TiO$_2$ and C/SnO$_2$NR, a plateau at E = 0.9 V was observed which can be assigned to the conversion reaction, followed by a sloping line until reaching the lower cut-off voltage due to the alloying reaction and SEI formation. In the case of SnO$_2$/C, the plateau due to the conversion reaction was not observed because it is probably covered by the Li$^+$ intercalation into the hard carbon matrix and the SEI formation.[42] During delithiation, in all three cases, three plateaus at E = 0.5 V, E = 1.3 V, and E = 1.9 V were observed and assigned to the de-alloying and oxidation reactions, respectively. At cycle 100, the shape of the E versus Q profiles was preserved despite the small capacity decay during cycling. The calculated dQ dE^{-1} versus E differential profiles clearly reflect the observations done for the E versus Q profiles, i.e., a sharp peak at E = 0.8 V, denoting the occurrence of the conversion reaction, followed by the broad peak at E = 0.2 V due to the alloying reaction were observed during the first lithiation. On delithiation, three peaks were observed at E = 0.5 V, E = 1.2 V, and E = 1.9 V assigned to the de-alloying and oxidation reaction, respectively. Furthermore, the dQ dE^{-1} versus E profiles are in good agreement with the results obtained by cyclic voltammetry. C/SnO$_2$NR showed the highest 1st coulombic efficiency among the three tested candidates (65.23%). This behavior can be tentatively explained by the morphology of SnO$_2$, which can favor electrolyte access and the kinetics of the conversion reaction. Indeed, in both cyclic voltammetries (Figure 4) and dQ dE^{-1} versus E profiles (Figure 5d,e) a larger peak **A** due to the conversion reaction and larger A' and A'' peaks for the oxidation reactions were observed. However, if that is the case, the smaller SnO$_2$ particle size would result in a larger specific surface area, which should lead to a larger surface available for the SEI formation and, thus, a larger irreversibility in the first cycle.

The three composite anode materials were further tested by a rate capability protocol with the purpose of determining how

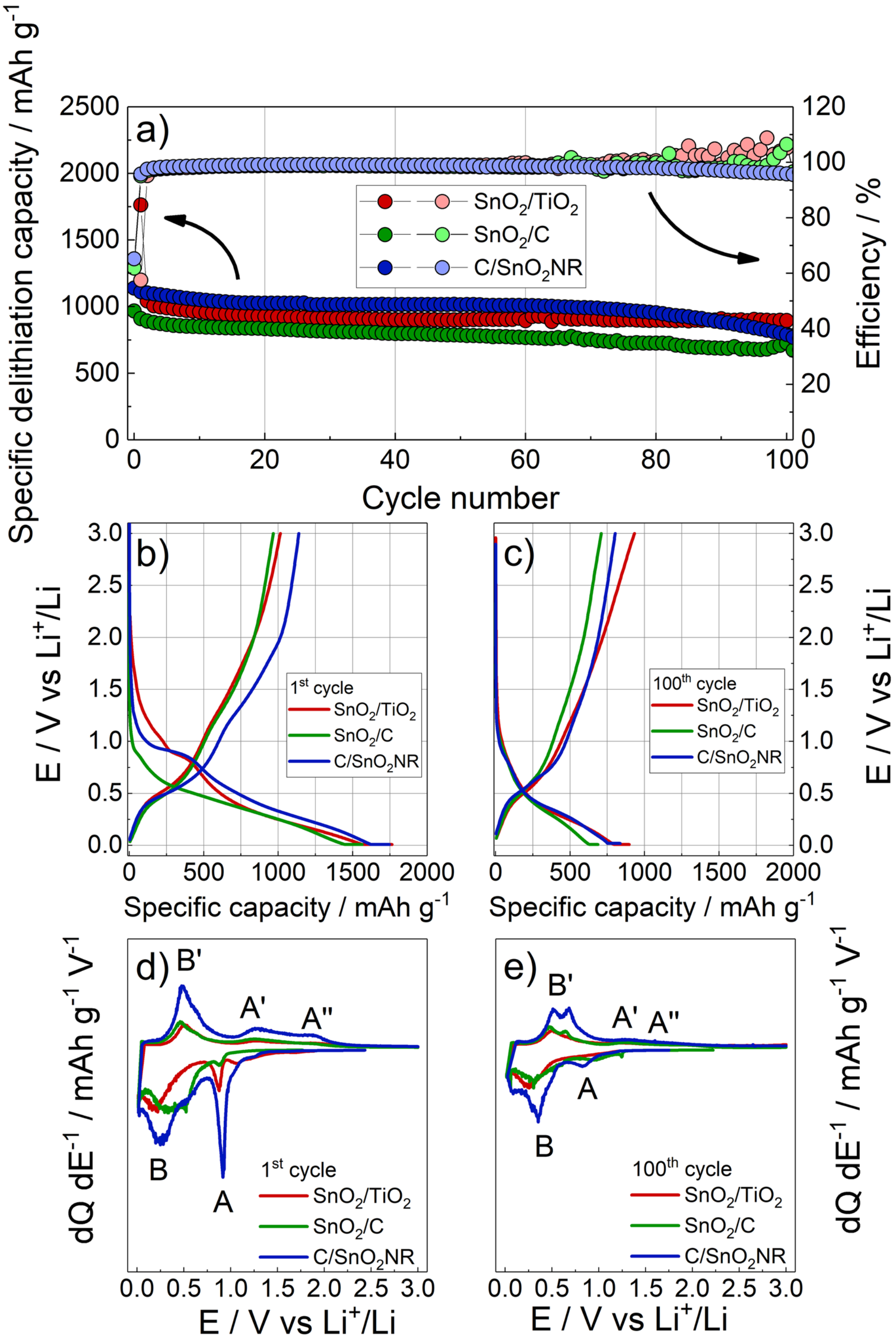

Figure 5. a) Specific capacity versus cycle number of the three tested composite anode materials. Galvanostatic profiles of the b) 1st cycle and b) the 100th cycle. Differential dQ dE^{-1} versus E profiles of the d) first cycle and e) the 100th cycle. CC-CV protocol with $I_{Spec} = 1$ A g^{-1} and $I_{CV} = 0.1$ A g^{-1} in the potential range within $0.010 < E < 3.000$ V versus Li$^+$/Li.

both the specific capacity and the average delithiation potential change with different current rates. The results are shown in **Figure 6**, and summarized in **Table 3**. As shown in Figure 6a, the test was performed by increasing the current rate, from 0.1 A g^{-1} up to 10 A g^{-1}, every 5 cycles. Thanks to the high SnO$_2$ content and small particle size, C/SnO$_2$NR showed the highest specific capacities when a current rate from 0.1 up to 5 A g^{-1} was applied. However, at 10 A g^{-1} SnO$_2$/C was the best anode material in terms of specific capacity, suggesting that at high current rates, not only the particle size, but also the overall

Table 2. Average specific capacity and initial coulombic efficiencies of SnO_2/TiO_2, SnO_2/C, and C/SnO_2NR obtained by galvanostatic cycling.

	First cycle lithiation capacity / mAh g^{-1}	First cycle coulombic efficiency / %	Average lithiation capacity in 100 cycles / mAh g^{-1}	Average coulombic efficiency / %
SnO_2/TiO_2	1763	57.49	908	99.82
SnO_2/C	1562	61.85	798	98.68
C/SnO_2NR	1744	65.23	1007	98.34

electronic conductivity of the active material plays an important role. In Figure S4a–f (Supporting Information), the galvanostatic profiles, as well as the dQ dE^{-1} versus E profiles at each current rate are reported. In the case of SnO_2/TiO_2 and C/SnO_2NR, at a low current rate, the galvanostatic E versus Q profiles are in good agreement with the results shown in Figure 5b,c; however, as the applied current increases the profiles progressively shrink. This issue is less pronounced in the case SnO_2/C in which

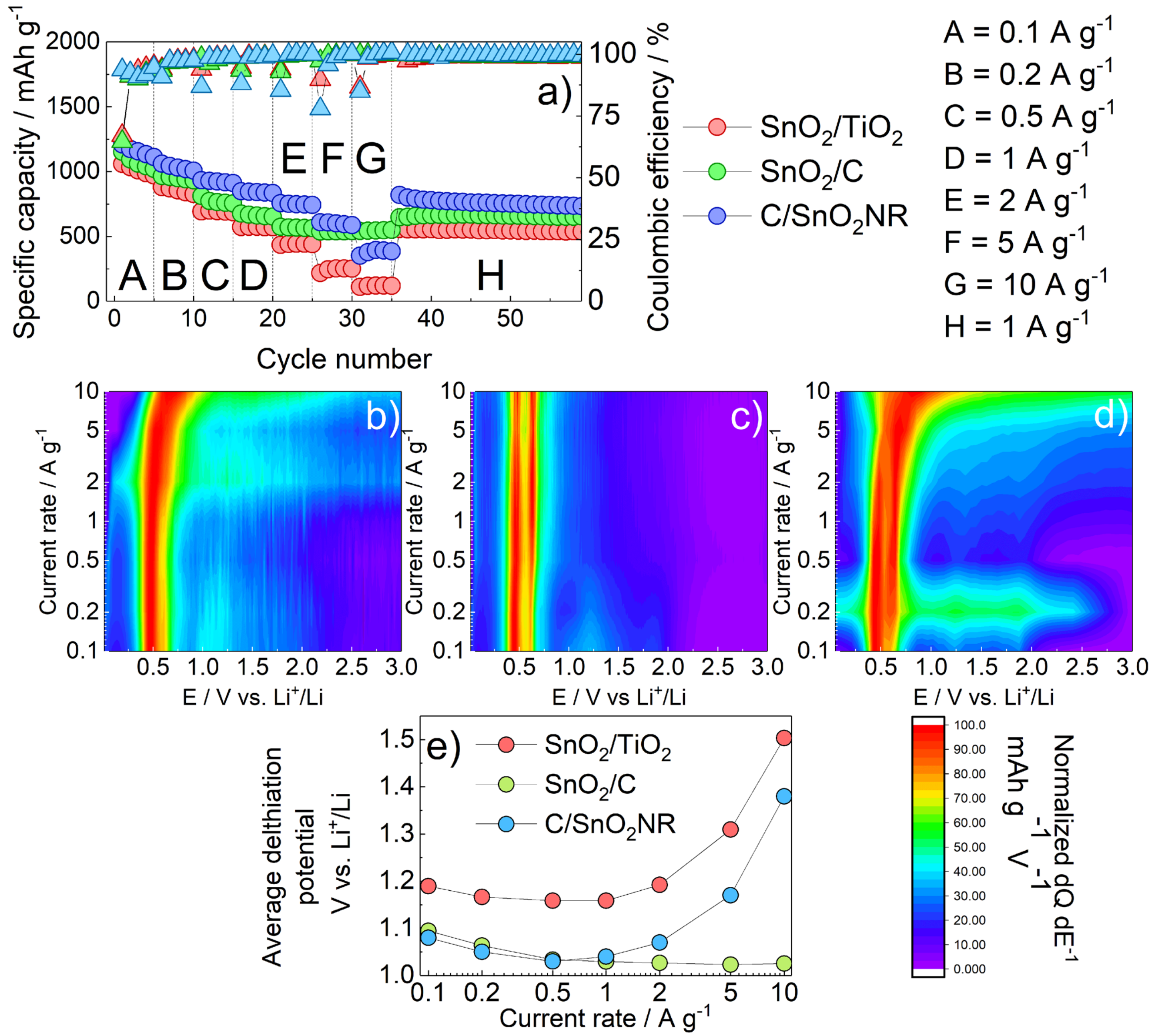

Figure 6. a) Rate capability test of SnO_2/TiO_2, SnO_2/C, and C/SnO_2NR. Contour plot of the differential dQ dE^{-1} versus E during delithiation of b) SnO_2/TiO_2, c) SnO_2/C, and d) C/SnO_2NR. e) Average delithiation potential versus applied current rate.

Table 3. Average delithiation capacity and coulombic efficiency at each current rate. Calculated average delithiation potential at each current rate.

Average delithiation capacity [mAh g^{-1}] / Average coulombic efficiency [%]

	0.1 A g^{-1}	0.2 A g^{-1}	0.5 A g^{-1}	1 A g^{-1}	2 A g^{-1}	5 A g^{-1}	10 A g^{-1}
SnO_2/TiO_2	Q = 1012 mAh g^{-1} / η = 90.95%	Q = 856 mAh g^{-1} / η = 97.01%	Q = 691 mAh g^{-1} / η = 98.23%	Q = 571 mAh g^{-1} / η = 99.23%	Q = 441 mAh g^{-1} / η = 99.95%	Q = 252 mAh g^{-1} / η = 99.44%	Q = 116 mAh g^{-1} / η = 99.95%
SnO_2/C	Q = 1060 mAh g^{-1} / η = 90.05%	Q = 945 mAh g^{-1} / η = 96.25%	Q = 763 mAh g^{-1} / η = 96.8%	Q = 664 mAh g^{-1} / η = 98.95%	Q = 567 mAh g^{-1} / η = 99.45%	Q = 543 mAh g^{-1} / η = 99.6%	Q = 531 mAh g^{-1} / η = 99.8%
C/SnO_2NR	Q = 1155 mAh g^{-1} / η = 94.28%	Q = 1027 mAh g^{-1} / η = 97.82%	Q = 920 mAh g^{-1} / η = 99.14%	Q = 845 mAh g^{-1} / η = 99.44%	Q = 746 mAh g^{-1} / η = 99.74%	Q = 595 mAh g^{-1} / η = 99.84%	Q = 377 mAh g^{-1} / η = 99.44%

Average delithiation potential [V]

	0.1 A g^{-1}	0.2 A g^{-1}	0.5 A g^{-1}	1 A g^{-1}	2 A g^{-1}	5 A g^{-1}	10 A g^{-1}
SnO_2/TiO_2	1.19 V	1.17 V	1.16 V	1.16 V	1.19 V	1.31 V	1.50 V
SnO_2/C	1.09 V	1.06 V	1.03 V	1.03 V	1.03 V	1.02 V	1.02 V
C/SnO_2NR	1.08 V	1.05 V	1.03 V	1.04 V	1.07 V	1.17 V	1.38 V

the E versus Q profiles slightly shrink while preserving the shape and plateau positions. These behaviors are reflected in the calculated differential dQ dE^{-1} versus E profiles (Figure S4d–f, Supporting Information), in which at a high current rate the conversion/oxidation peaks of SnO_2/TiO_2 and C/SnO_2NR were not observed. Furthermore, an appreciable shift of the de/alloying peaks due to the polarization was observed, while in the case of SnO_2/C the peaks position and, thus, the redox potential was almost unaltered by the current changes.

To shed light and better visualize the electrochemical properties of the proposed materials in terms of power capability, contour plots of the dQ dE^{-1} versus E profiles during delithiation were calculated (Figure 6b–d). In this way, the average voltage during delithiation (or discharge of a full cell) can be graphically estimated. The composites SnO_2/TiO_2 and C/SnO_2NR performed in a similar way, having most of the capacity delivered at E = 0.5 V, where the alloying reaction occurs, and shifting to higher potential values when current rates of 5 and 10 A g^{-1} were applied. In the case of SnO_2/C, no potential shifts because of polarization were detected, suggesting that the high content of amorphous carbon can effectively mitigate this issue.

Furthermore, the average voltage during delithiation was calculated for each current rate by applying the following equation Equation (4):

$$\bar{U}_{\text{del}} = \frac{\int_0^{t_f} U(t)\,dt}{t_f} \tag{4}$$

where $\bar{U}$ is the average delithiation potential and t_f is the time duration of the half cycle. The results are shown in Figure 6e. As for the results shown in Figure 6b–d, the lower the voltage the better the power capability of the composite anode materials. SnO_2/TiO_2 showed the worst performance, reaching average potential values of 1.31 and 1.50 V versus Li^+/Li at 5 and 10 A g^{-1}, respectively. This behavior can be attributed to the low content of carbon in the composite and to the presence of TiO_2 which possesses a low electronic conductivity (≈10^{-10}–10^{-11} S cm^{-1}).[43] C/SnO_2NR performed in a similar way, with the average potential values increasing in the last two current rates tested. Notably, both composites showed an initial decrease of the average potential, with a local minimum at 1 A g^{-1} followed by an increase at the higher current rates. This feature can be attributed to the more pronounced conversion reaction at low current rates, which can be visually estimated in Figure 6b,c, with the light green region at E > 0.5 V.

2.3. Interfacial and Transport Properties Characterization

To investigate the interfacial and transport properties of the three composite anode materials, cyclic voltammetries at different scan rates, galvanostatic intermittent titration technique (GITT), and potentiostatic electrochemical impedance spectroscopy (PEIS) were employed. The results of the cyclic voltammetries at different scan rates are reported in **Figure 7**. 10 different scan rates within 50 and 500 µV s^{-1} and with increments of 50 µV s^{-1} were employed. As clearly depicted in Figure 7a–c, with the increase of the voltage step width the measured current increases, as expected, suggesting a diffusion-controlled behavior.

In Figure 7d–f, the intensity of the alloying peak during lithiation versus the square root of the sweep rate is reported. In all three cases, there is a linear relationship between the peak current and $\nu^{(1/2)}$ as demonstrated by the R^2 coefficient of the linear regression ($R^2 = 0.99787$, $R^2 = 0.99798$, and $R^2 = 0.98109$ for SnO_2/TiO_2, SnO_2/C, and C/SnO_2NR, respectively). This feature confirms a diffusion-controlled mechanism as provided by the Randles-Sevcik equation[44] Equation (5):

$$i_p = 0.4463 nFAC \left(\frac{nF\nu D_{Li}}{RT} \right)^{\frac{1}{2}} \tag{5}$$

where i_p, n, F, A, C, R, T, and D are the peak intensity, the number of exchanged electrons, the Faraday's constant, the surface area of the electrode, the concentration of Li^+ in the active material, the gas constant, the sample temperature, and the Li diffusion coefficient in the active material.[44] The slope of the linear fit can graphically represent the diffusion coefficient, with

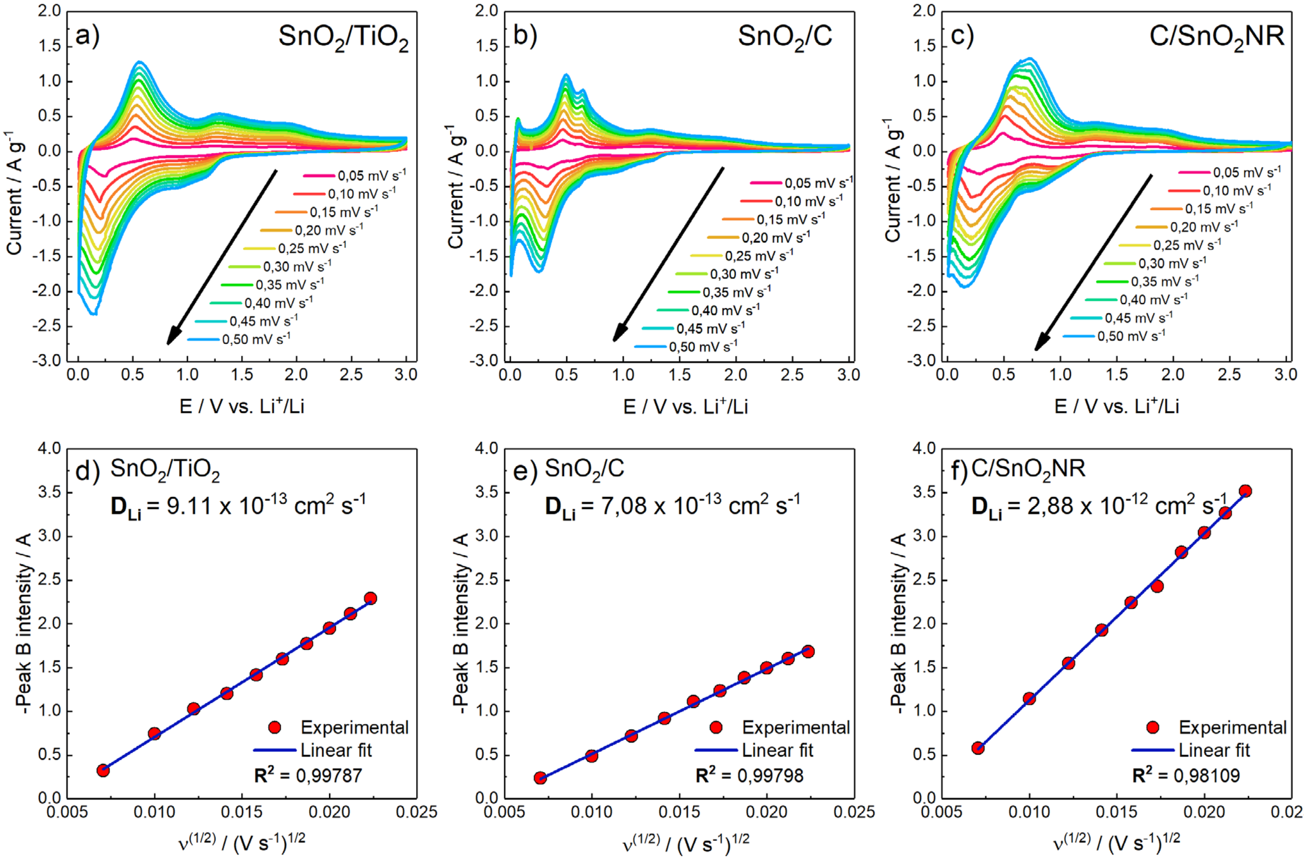

Figure 7. Cyclic voltammetry at different scan rates of a) SnO_2/TiO_2, b) SnO_2/C, and c) C/SnO_2NR. Peak intensity versus $\nu^{(1/2)}$ and the corresponding linear fit of d) SnO_2/TiO_2, e) SnO_2/C, and f) C/SnO_2NR.

higher slope values indicating higher the Li apparent diffusion coefficient. C/SnO_2NR has shown the highest slope and, thus, the highest Li apparent solid-state diffusion coefficient among the three tested composite materials, with a $D_{App,Li} = 2.88 \times 10^{-12}$ cm^2 s^{-1} versus 9.11×10^{-13} cm^2 s^{-1} and 7.08×10^{-13} cm^2 s^{-1} for SnO_2/TiO_2 and SnO_2/C, respectively. This feature can be explained by the smaller particle size of C/SnO_2NR (≈40 nm) compared to the first two composites (≈100 nm); indeed, it can be translated in a shorter diffusion path and could explain the better electrochemical performance such as the higher specific capacity and the better rate capability. These results agree with the calculated $D_{App,Li}$ obtained from GITT in **Figure 8**.

The electrodes were cycled 4 times with a specific current of 100 mA g^{-1} prior to the GITT measurement to allow the formation of a stable SEI. The titration was performed by applying a specific current of 100 mA g^{-1} for 10 min followed by a relaxation of 2 h to ensure the reaching of the equilibrium potential. All three measurements (Figure 8a–c) are characterized by the step-like curve in which the end of each rest step represents the equilibrium potential for the calculation of the Li diffusion coefficient. The apparent D_{Li} was calculated according to the formula[45] Equation (6):

$$D_{Li} = \frac{4}{\pi}\left(I_0\frac{V_m}{FS}\right)^2\left(\frac{dE}{d\delta}/\frac{dE}{dt^{1/2}}\right)^2, t \ll L^2/D_{Li} \qquad (6)$$

where D_{Li}, I_0, V_m, F, S, and L are the lithium diffusion coefficient, the applied current, the molar volume of active material, the Faraday's constant, the electrode surface area, and the thickness of the film. $dE/d\delta$ is the slope in the E versus δ plot reported in Figure S5a (Supporting Information), while $dE/dt^{1/2}$ is the slope in the E versus $t^{1/2}$ plot (calculated for each GITT step) reported in Figure S5b (Supporting Information). C/SnO_2NR has shown the highest $D_{App,Li}$ among the three composite anode materials, confirming the results obtained by the cyclic voltammetry at different scan rates. Thus, a tailored morphology coupled to a small particle size can effectively improve the apparent lithium diffusion coefficient and, eventually, the electrochemical performances. Interestingly, all the curves in Figure 8d–f seem to have six local minima upon lithiation which, as suggested by R.A. Huggins,[46] can be indexed to the formation of three-phases equilibria between Li_2O, a lithiated $Li_\delta Sn$ phase, and the next $Li_{\delta+\gamma}Sn$ lithiated phase. However, to confirm these results, further measurements such as in-/ex-situ X-ray spectroscopy and in-/ex-situ X-ray diffraction are needed and will be subject to future work. The results are summarized in **Table 4**.

The interfacial behavior at the electrode/electrolyte interface was studied by using potentiostatic electrochemical impedance spectroscopy (PEIS). In addition, the impedance measurements were performed with the sole purpose of assessing the stability of the composite electrodes upon cycling. Indeed, the resistance of the charge-transfer process, and thus the

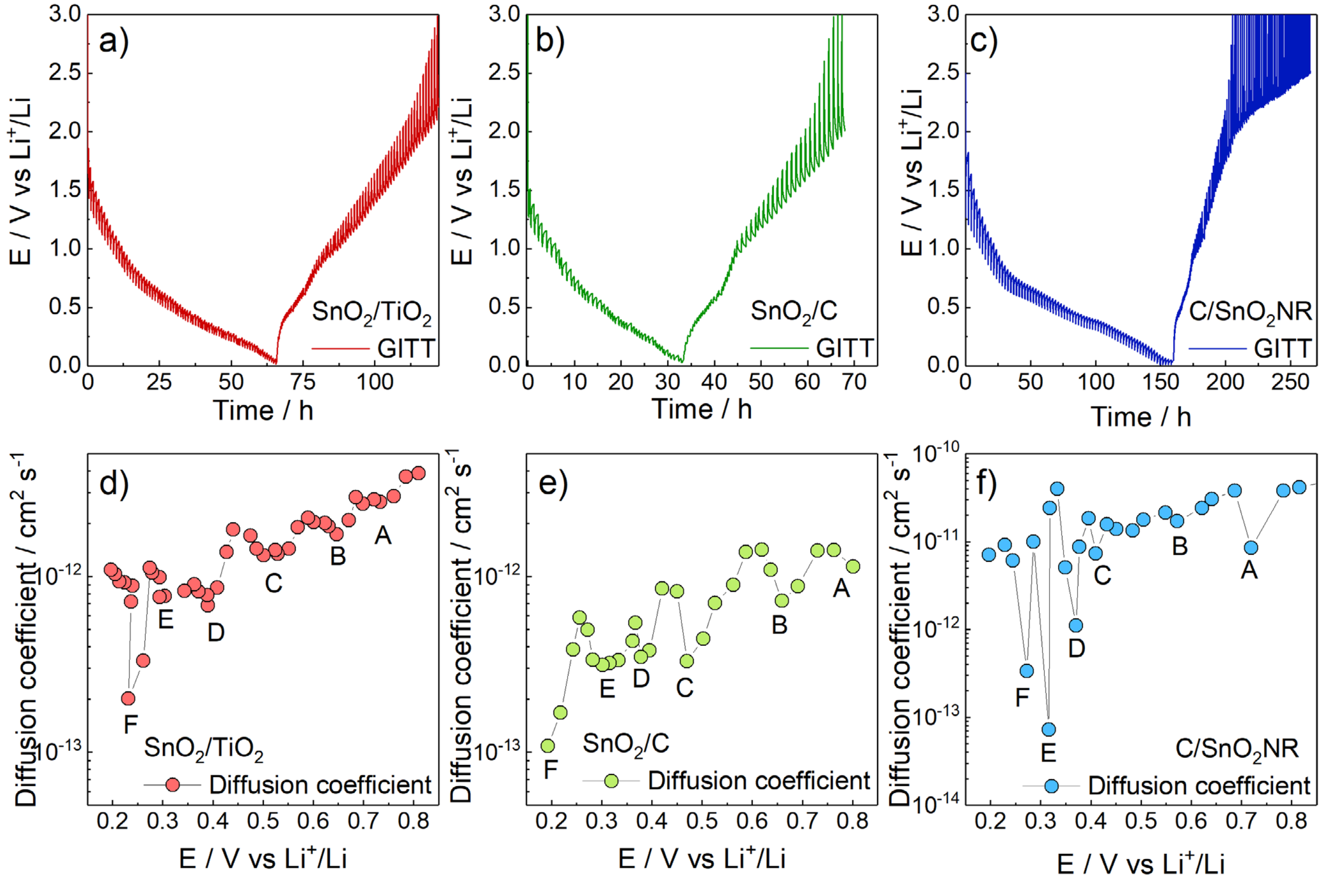

Figure 8. GITT curve of a) SnO_2/TiO_2, b) SnO_2/C, and c) C/SnO_2NR. Calculated D_{Li} during lithiation of d) SnO_2/TiO_2, e) SnO_2/C, and f) C/SnO_2NR.

overall impedance, is strictly dependent on the state-of-charge of the electrode materials[47]; even though all the PEIS measurements were performed at the same potential value, the state-of-charge of each composite material is slightly different, as shown in Figure 5. Briefly, ac-responses were acquired every 10th galvanostatic cycle ($I = 1$ A g^{-1}) at the bias potential $E = 0.2$ V with a perturbation amplitude of $\Delta E = \pm 5$ mV. All the cells were held at $E = 0.2$ V versus Li^+/Li prior to the PEIS acquisition in order to ensure the equilibrium condition.[48] All the ac-dispersions are characterized by four common features, i.e.: an intercept in the real axis due to the conduction of charges in the electrolyte, an arc in the high-frequency region due to the passivation layer (SEI), a medium frequency arc due to the charge transfer resistance coupled to the double layer capacitance and, at last, a low-frequency polarization line due to the diffusion of Li into the active material. At first sight, SnO_2/TiO_2 showed a much higher impedance compared to the other two composite anode materials. This feature can be explained by i) the low content of carbon in the composite compared to SnO_2/C, ii) the presence of TiO_2 which possesses a low electronic conductivity,[35] and iii) larger SnO_2 particle size compared to C/SnO_2NR. In all three cases, as the cell is aged through galvanostatic cycling, the ac-dispersions slowly shift to the right and increase in magnitude, suggesting a slight degradation of the electrolyte and degradation of the electrode and/or the electrode/electrolyte interface. To shed light on the interfacial behavior of the proposed composites, the impedance spectra were fit by using CNLS-fit (Relaxis 3 software, RHD instruments) with the equivalent circuit model shown in the first row of **Figure 9**. The used ECM $R_{el}(R_{SEI}C_{SEI})([R_{ct}\ W]Q_{dl})$ (written in Boukamp's notation)[49] is constituted by a pure resistor element R_{el} to model the conduction of charges through the electrolyte, an $R_{SEI}C_{SEI}$ parallel to model the SEI layer in the anode,

Table 4. Summary of the three-phase equilibria in the D_{Li} versus E plot measured by GITT.

	Potential / V vs Li^+/Li	Three-phases equilibrium
A	0.85–0.75 V	Li_2O-Sn-$Li_{0.4}Sn$
B	0.65–0.60 V	Li_2O-$Li_{0.4}Sn$-$Li_{0.714}Sn$
C	0.55–0.40 V	Li_2O-$Li_{0.714}Sn$-$Li_{2.33}Sn$
D	0.40–0.35 V	Li_2O-$Li_{2.33}$-$Li_{2.6}Sn$
E	0.35–0.30 V	Li_2O-$Li_{2.6}Sn$-$Li_{3.5}Sn$
F	0.35–0.20 V	Li_2O-$Li_{3.5}Sn$-$Li_{4.4}Sn$

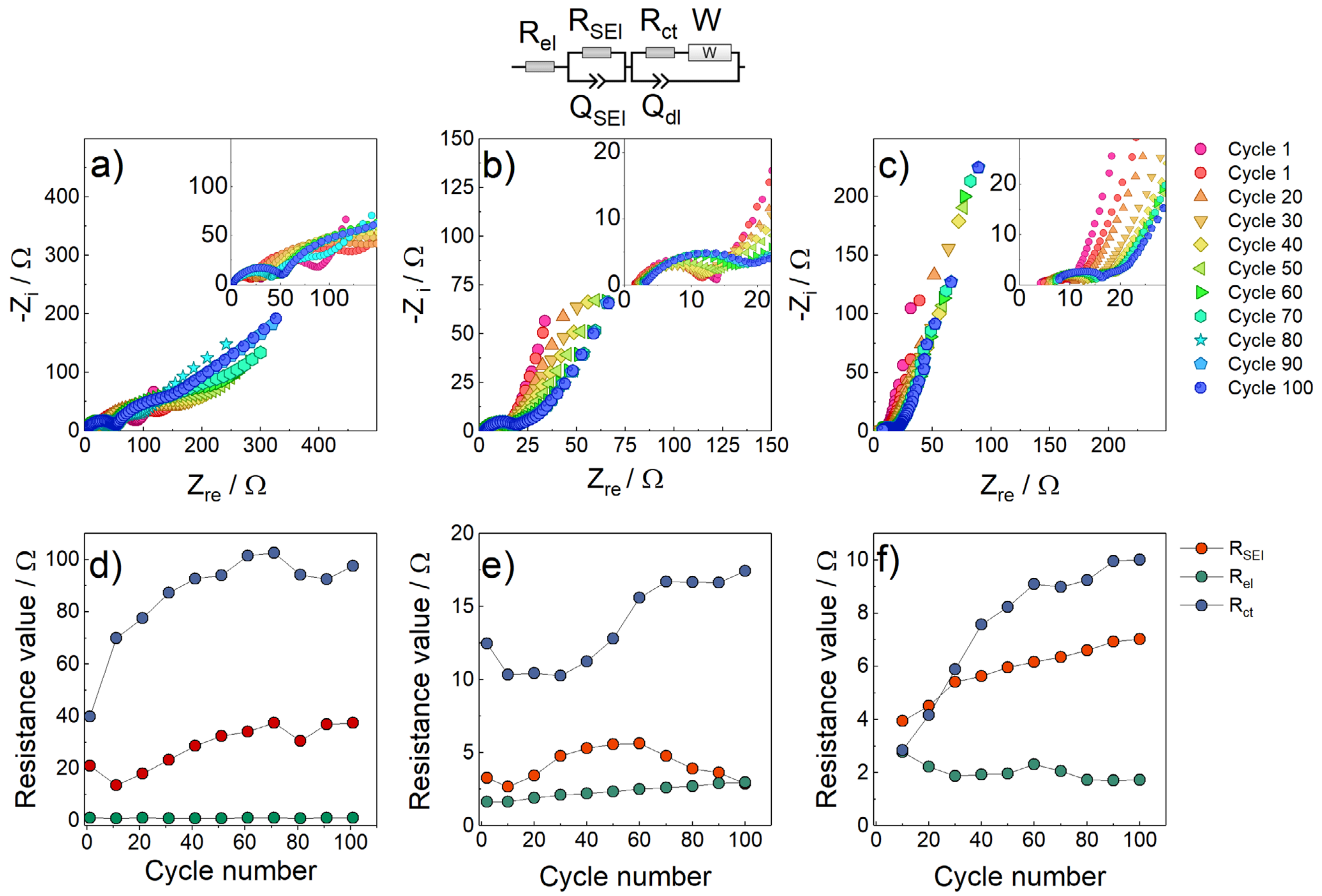

Figure 9. First row: Equivalent circuit model used for the CNLS-fit of the obtained ac-responses. Nyquist plot acquired every 10 cycles of a) SnO_2/TiO_2, b) SnO_2/C, and c) C/SnO_2NR. Calculated resistance value obtained by CNLS-fit of the Nyquist plot of d) SnO_2/TiO_2, e) SnO_2/C, and f) C/SnO_2NR.

and a $[R_{ct}W]C_{dl}$ to model the charge transfer process coupled to the electrical double layer with the Warburg element to model the semi-infinite diffusion. During the fit procedure, all the capacitor elements were replaced by a constant phase element (Q in Boukamp's notation) to consider electrode inhomogeneities and roughness.[48] The calculated resistance values versus cycle number are shown in Figure 9d–f. In the case of SnO_2/TiO_2, a slight increase in the resistance associated with the SEI layer was observed. This feature can be explained by the continuous structural and morphological evolution of the active material, which could expose a fresh surface to the formation of a new passivation layer as well as the thickening of the already existing one. On the other hand, the resistance associated with the charge-transfer process sharply increases in the first 40 cycles, for then reaching stable values around 100 Ω. This behavior can be again explained by the recurrent structural and morphological evolution of the anode material as well as the agglomeration and migration of the Sn particles to the electrode surface.[13,38] A slight increase of the electrolyte resistance was observed in the case of SnO_2/C, suggesting a slight decomposition of the electrolyte and/or a slight cell swelling. The R_{SEI} of SnO_2/C slightly increases in the first 50 cycles for then decreases until reaching its original values. Such a trend can be tentatively ascribed to a possible thickening of the SEI layer in the first 50 cycles, for then having a redistribution over the surface of the active material in the last 50 cycles.[13] At last, the R_{ct} of SnO_2/C was stable at ≈10 Ω for the first 50 cycles for then increased> 15 Ω, suggesting that the applied carbon scaffold was able to mitigate the mechanical stresses in the electrode for at least the first 50 cycles.

In the case of C/SnO_2NR, the lowest impedance values were observed among the three composites. The resistance associated with the electrolyte experienced only small fluctuations during 100 cycles, while in the case of R_{SEI} a steady growth was observed, probably due to exposure to a fresh surface for a further electrolyte decomposition given by the continuous structural and morphological rearrangement of the active material. Concerning R_{ct}, an increase from ≈20 up to ≈10 Ω was observed in the first 60 cycles which, again, can be associated with the morphological and structural evolution of the electrode material.

3. Conclusion

In this work, three different composite anode materials based on SnO_2 have been synthesized and thoroughly characterized. All the reported materials showed stable and high specific capacities (almost three times higher than that of graphite); however, they have shown intrinsically different properties mainly due to the different strategies used for the stabilization of SnO_2.

When stabilized with an inorganic matrix (SnO_2/TiO_2) a high and stable specific capacity of ≈ 900 mAh g^{-1} is obtained; however, the presence of an almost insulating material such as TiO_2 led to poorer rate capability and larger overall impedance compared to the other tested materials. The galvanostatic intermittent titration technique revealed an apparent Li^+ diffusion coefficient in the range of 10^{-13}–10^{-11} cm^2 s^{-1}, in agreement with literature values, with six local minima due to the formation of three-phases equilibrium between Li_2O, a lithiated $Li_\delta Sn$ phase, and the next $Li_{\delta+\gamma}Sn$ lithiated phase. A similar apparent diffusion coefficient was obtained with cyclic voltammetry at different scan rates (9.11×10^{-13} cm^2 s^{-1}).

SnO_2/C has shown a slightly different redox behavior when compared with the other tested materials. This is due to the larger amount of carbon used for the stabilization, i.e., 44.04% in SnO_2/C versus 12.44% and 11.64% in SnO_2/TiO_2 and C/SnO_2NR, respectively. The reduction peak (both in cyclic voltammetry and in the differential galvanostatic dQ dE^{-1} vs E profiles) associated with the conversion reaction has shown a lower intensity due to the simultaneous lithiation of the hard carbon matrix. For this reason, a lower specific capacity of ≈800 mAh g^{-1} was measured. The measured apparent diffusion coefficient given by cyclic voltammetry and galvanostatic intermittent titration technique has similar values and trends with SnO_2/TiO_2 as expected since both composites were prepared with the same SnO_2 nanopowder. However, thanks to the larger amount of carbon (44.04%) compared with the other two composite anode materials, the materials has shown a better capacity retention at the current rate of 5 A g^{-1} and 10 A g^{-1}. On the other hand, when smaller SnO_2 particles (Ø < 100 nm) arranged in a nanorod shape (C/SnO_2NR) are used, the highest specific capacity of ≈1000 mAh g^{-1} was obtained. Thanks to the smaller particle size, a higher apparent diffusion coefficient was measured (2.88×10^{-12} cm^2 s^{-1} by CV and between 10^{-13}–10^{-10} cm^2 s^{-1} by GITT) which can explain the satisfactory rate response. Furthermore, as highlighted by EIS measurements, the C/SnO_2NR electrodes have the lowest overall impedance thanks to the morphology of the active material. In addition, in all three cases, a worsening of the charge-transfer kinetic and the electrode/electrolyte interface was observed due to the well-known structural rearrangements and volume expansion of SnO_2-based anodes.

In summary, the different strategies adopted for the stabilization of SnO_2-based materials greatly affect the electrochemical behavior and performance of the anode. Larger amounts of hard carbon (SnO_2/C) led to a lower specific capacity; however, as shown by the rate capability test, the material demonstrated better capacity retention at high current rates. Using TiO_2 as a buffering matrix leads to a slightly higher specific capacity compared to SnO_2/C, given by the higher amount of SnO_2 in the composite. However, due to the insulating nature of TiO_2, the material has shown the worst rate capability and the highest overall impedance. The use of a tailored morphology can stabilize the charge/discharge behavior as demonstrated with C/SnO_2NR. In addition, only a lower amount of carbon (11.64%) is needed to stabilize the SnO_2. In this regard, C/SnO_2NR has shown the highest specific capacity, a modest rate capability, and the lowest overall impedance.

4. Experimental Section

Materials: SnO_2 nanopowder (≤100 nm avg. part. size), polyacrylic acid polymer binder (PAA, m.w. = 450 000 g mol^{-1}), sucrose (≥99.5% (GC)), Tin oxalate (SnC_2O_4, 98%), Titanium (IV) isopropoxide (Technipur, for synthesis), ethylene glycol (ReagentPlus, ≥99%), NH_4OH (ACS reagent, 28.0-30.0% NH_3 basis), and Lithium (99.9% trace metals basis) were acquired form Sigma-Aldrich (Merck S.p.A., Milan, Italy) and used as received.

Super C65 carbon and 1 м $LiPF_6$ in ethylene carbonate:dimethyl carbonate (EC:DMC 1:1 vol) + 2% vinylene carbonate electrolyte solution (2% VC) were acquired from Timcal C-Energy (Paris, France) and Solvionic (Tolouse, France), respectively, and used without any further purification.

Whatman GF/A glass fiber separators were acquired from Sigma-Aldrich and dried at 270 °C for 72 h in a Büchi vacuum oven (Büchi B-585) before transferring inside the glovebox.

Synthesis of SnO_2/TiO_2: SnO_2 nanopowder was dispersed in isopropanol by ultrasonic treatment (50 W power-continuous mode, Hielscher UP100H, Teltow, Germany) to achieve a homogeneous dispersion. Triton X-100 was added as a capping agent[50] and magnetic stirring was maintained for 2 h. Titanium (IV) isopropoxide (Sigma-Aldrich) was added and the temperature was raised to 80 °C. Eventually, aqueous ammonia solution (30% v/v) and ultrapure water were added dropwise to the solution, and the formation of a pale-yellow precipitate was observed. After the solvent evaporation overnight at T = 70 °C, the powder was treated in a tubular furnace at 600 °C for 4 h under Ar atmosphere (thermal gradient: 5 °C min^{-1}, Q_{Ar} = 1 L min^{-1}) to obtain Anatase crystal phase.[51] The weight ratio between SnO_2 and TiO_2 is 3:1.

Synthesis of SnO_2/C: SnO_2/C was synthesized following a simple and fast procedure. First, a certain amount of sucrose was dissolved in ethanol. Then, commercial SnO_2 nanopowder was dispersed into the above solution with the help of an ultrasonic immersion stirrer (50 W power-continuous mode, Hielscher UP100H, Teltow, Germany), considering a final ratio of SnO_2:C 1:1. After 1 h the dispersion was heated at 70 °C until complete evaporation of the solvent. The obtained powder was ball-milled (Retsch S100 planetary ball mill) by using an Agata jar and Agata spheres of Ø = 10 mm (ball to powder weight ratio 10:1) at 400 rpm for 2 h. Eventually, the powder was collected and treated in a tubular furnace at 600 °C for 4 h under an Ar atmosphere (thermal gradient: 5 °C min^{-1}, Q_{Ar} = 1 L min^{-1}) to obtain the amorphous carbon matrix.

Synthesis of C/SnO_2NR: SnO_2 nanorods have been synthesized by a modified polyol-mediated oligomerization of SnC_2O_4 nanowires.[52–54] Briefly, 200 mL of ethylene glycol were heated at T = 160 °C. Afterward, 2 g of SnC_2O_4 and 1 g of Pluronic P123 were dissolved in EG. The solution was left at T = 160 °C for 12 h. Eventually, the powder was collected by centrifugation and thoroughly washed with u.p. H_2O and EtOH. The SnC_2O_4 was finally converted into SnO_2 by thermal annealing in a tube furnace at 500 °C for 4 h (ramping rate = 1 °C min^{-1}, Q_{air} 1 L min^{-1}).

The carbon coating was prepared by dehydration of sucrose in the presence of H_2SO_4. SnO_2 nanorods were dispersed in a solution of sucrose in u.p. water (sucrose: SnO_2 ratio of 3:1). Then, 10 µL of conc. H_2SO_4 was added to the above solution and heated at T = 100 °C for 4 h. Eventually, the temperature was raised to T = 160 °C until the solution was evaporated. The powder was then collected, grounded, and eventually treated in a tube furnace at T = 600 °C for 4 h in Ar atmosphere (ramping rate = 1 °C min^{-1}, Q_{Ar} 1 L min^{-1}).

Structural and Morphological Characterization: The structure of the SnO_2 composite powders was determined by Raman scattering and X-ray diffraction. A Horiba iH320 Raman spectrometer equipped with a 532 nm laser source, and a Philips diffractometer equipped with a Cu-Kα source (λ = 1.540 Å) were used, respectively. The morphology of the samples was assessed by a field-emission scanning electron microscope from Zeiss (Zeiss Sigma series 300).

Thermal Characterization: The carbon content was quantified by using a Perkin-Elmer STA6000 TGA-DTA, from r.t. up to 800 °C with a rate of 10 °C min^{-1} in air atmosphere (10 mL min^{-1}).

Electrode Processing: The electrode layers were prepared by doctor blade technique. All the slurries were prepared with the same formulation of 70:20:10 of active material, conductive carbon additive (Super C65 carbon), and binder (polyacrylic acid, PAA), respectively. First, the binder PAA was dissolved in ethanol to obtain a 5% solution. To ensure proper electronic contact, the active material and the carbon additive were finely ground in an agate mortar before adding them to the slurry. The mixed powders were then added to the binder solution reaching a solid content of ≈ 40% and stirred for 12 h. Eventually, the slurries were cast onto copper foil (MSE supplies, thickness = 9 µm) with a blade gap of 150 µm. The electrode layers were then dried at 70 °C for 2h. Circular electrodes of Ø = 9 mm were cut using an electrode puncher (EL-Cut, EL-CELL). Eventually, the electrodes were pressed at 4.7 tons cm^{-2}, weighted, and vacuum dried at 120 °C for 12 h before transferring to the glovebox. The average loading of active material was ≈1.5 mg cm^{-2}.

Electrochemical Characterization: Three-electrode cells have been used for the electrochemical characterization employing the active material as working electrode, and Li metal as both counter and reference electrodes. 1 м LiPF_6 in EC:DMC (1:1 v:v) + 2% VC was used as electrolyte, and Whatman GF/A glassfiber discs as separator (Ø = 12 mm). Swagelok-type cells were used for Cyclic Voltammetry (CV), Galvanostatic Cycling (GC), Rate Capability (RC), and GITT. Prior to any electrochemical characterization, an open circuit voltage period of 12 h was used. Cyclic voltammetry was acquired from a scan rate of 50 up to 500 µV s^{-1} with 50 µV s^{-1} increment steps. Galvanostatic cycling experiments were performed by applying specific currents ranging from 0.1 up to 10 A g^{-1}. ECC-REF cells (EL-CELL gmbh, Hamburg, Germany) were used for Potentiostatic Electrochemical Impedance Spectroscopy (PEIS). Impedance spectra were acquired every 10th cycle at selected bias potential E = 0.2 V by applying a sinusoidal voltage perturbation of $\Delta E \pm 5$ mV in the frequency domain $7\text{ mHz} < f < 200\text{ kHz}$, and with 10 points per decade in logarithmic spacing. All the electrochemical measurements have been performed in the potential window $0.010\text{ V} < E < 3.000\text{ V}$. If not stated, all the potential values are referred to as the Li^+/Li redox couple (−3.041 V vs SHE).

The specific capacities were calculated according to the mass of the composite active material as shown in Equations (7–9):

$$\text{Specific capacity }\left(\text{mAh g}^{-1}\right) = \frac{\text{measured capacity (mAh)}}{\text{SnO}_2/\text{TiO}_2\text{ mass (g)}};\ \text{for SnO}_2/\text{TiO}_2 \tag{7}$$

$$\text{Specific capacity }\left(\text{mAh g}^{-1}\right) = \frac{\text{measured capacity (mAh)}}{\text{C/SnO}_2\text{ mass (g)}};\ \text{for C/SnO}_2 \tag{8}$$

$$\text{Specific capacity }\left(\text{mAh g}^{-1}\right) = \frac{\text{measured capacity (mAh)}}{\text{C/SnO}_2\text{NR mass (g)}};\ \text{for C/SnO}_2\text{NR} \tag{9}$$

All the cell assembly procedures were carried out inside an Ar-filled glovebox (Jacomex GP-Campus, Dagneoux, France) with H_2O and O_2 levels < 1 ppm. All the electrochemical measurements have been performed on a VMP-3 multichannel galvanostat/potentiostat/FRA (Bio-Logic, Seyssinet-Pariset, France).

Supporting Information

Supporting Information is available from the Wiley Online Library or from the author.

Acknowledgements

The support of ENEA and MiSE (Agenzia Nazionale per le Nuove Tecnologie, l'Energia e lo Sviluppo Sostenibile e Ministero per lo Sviluppo Economico) is gratefully acknowledged under the Project "Sistemi di Accumulo di Energia per il Sistema Elettrico", funded by PAR2019-2021 Program. This study was carried out within the MOST e Sustainable Mobility Center and received funding from the European Union Next-GenerationEU (PIANO NAZIONALE DI RIPRESA E RESILIENZA (PNRR) e MISSIONE 4 COMPONENTE 2, INVESTIMENTO 1.4 e D.D. 1033 17/06/2022, CN00000023). This manuscript reflects only the authors' views and opinions, neither the European Union nor the European Commission can be considered responsible for them. Prof. Jusef Hassoun and Dr. Vittorio Marangon are kindly acknowledged for the TEM measurements.

Open access publishing facilitated by Universita degli Studi di Bologna, as part of the Wiley - CRUI-CARE agreement.

Conflict of Interest

The authors declare no conflict of interest.

Data Availability Statement

The data that support the findings of this study are available from the corresponding author upon reasonable request.

Keywords

anode, composite, li-ion batteries, nanomaterials, tin oxide

Received: December 6, 2024
Revised: March 28, 2025

[1] X. Zeng, M. Li, D. A. El-Hady, W. Alshitari, A. S. Al-Bogami, J. Lu, K. Amine, *Adv. Energy Mater.* **2019**, *9*, 1900161.
[2] L. Weimer, T. Braun, A. vom Hemdt, *Resour. Policy* **2019**, *64*, 101473.
[3] M. Malik, K. H. Chan, G. Azimi, *Mater. Today Energy* **2022**, *28*, 101066.
[4] P. Stüble, V. Mereacre, H. Geßwein, J. R. Binder, *Adv. Energy Mater.* **2023**, *13*, 2203778.
[5] S. Levchenko, S. Wei, V. Marangon, J. Hassoun, *Energy Technol.* **2022**, *10*, 2200725.
[6] L. Minnetti, V. Marangon, J. Hassoun, *Adv. Sustain. Syst.* **2022**, *6*, 2100464.
[7] Y. Deng, C. Yang, K. Zou, X. Qin, Z. Zhao, G. Chen, *Adv. Energy Mater.* **2017**, *7*, 1601958.
[8] L. Sun, Y. Liu, R. Shao, J. Wu, R. Jiang, Z. Jin, *Energy Storage Mater.* **2022**, *46*, 482.
[9] L. Sun, Y. Liu, J. Wu, R. Shao, R. Jiang, Z. Tie, Z. Jin, L. Sun, Y. Liu, J. Wu, R. Shao, R. Jiang, Z. Tie, Z. Jin, *Small* **2022**, *18*, 2102894.
[10] M. Grohol, C. Veeh, DG GROW, European Commission, *Study on the Critical Raw Materials for the EU 2023 Final Report* **2023**.
[11] A. Kraytsberg, Y. Ein-Eli, *A critical review-promises and barriers of conversion electrodes for Li-ion batteries*, Vol. *21*, Springer, New York LLC, **2017**, pp. 1907–1923.
[12] S. Liang, Y.-J. Cheng, J. Zhu, Y. Xia, P. Müller-Buschbaum, S. Liang, P. Müller-Buschbaum, Y. Cheng, J. Zhu, Y. Xia, P. Müller-Buschbaum Heinz Maier-Leibnitz Zentrum, *Small Methods* **2020**, *4*, 2000218.
[13] R. Hu, D. Chen, G. Waller, Y. Ouyang, Y. Chen, B. Zhao, B. Rainwater, C. Yang, M. Zhu, M. Liu, *Energy Environ. Sci* **2016**, *9*, 595.

[14] A. Birrozzi, J. Asenbauer, T. E. Ashton, A. R. Groves, D. Geiger, U. Kaiser, J. A. Darr, D. Bresser, *Batter. Supercaps* **2020**, *3*, 284.

[15] A. Birrozzi, S. P. Bautista, J. Asenbauer, T. Eisenmann, T. E. Ashton, A. R. Groves, C. Starkey, J. A. Darr, D. Geiger, U. Kaiser, G. T. Kim, M. Weil, D. Bresser, *Adv. Mater. Technol.* **2022**, *7*, 2200353.

[16] I. Ostroman, C. Ferrara, S. Marchionna, A. Gentile, N. Vallana, D. Sheptyakov, R. Lorenzi, R. Ruffo, *Small Methods* **2023**, 2300503.

[17] S. Gao, N. Wang, S. Li, D. Li, Z. Cui, G. Yue, J. Liu, X. Zhao, L. Jiang, Y. Zhao, *Angew. Chem., Int. Ed.* **2020**, *59*, 2465.

[18] H. Mou, Y. Xin, C. Miao, S. Nie, S. Chen, W. Xiao, *Electrochim. Acta* **2021**, *397*, 139286.

[19] A. Gentile, S. Arnold, C. Ferrara, S. Marchionna, Y. Tang, J. Maibach, C. Kübel, V. Presser, R. Ruffo, *Adv. Mater. Interfaces* **2023**, *10*, 2202484.

[20] C. Gao, Z. Jiang, P. Wang, L. R. Jensen, Y. Zhang, Y. Yue, *Nano Energy* **2020**, *74*, 104868.

[21] Y. Xin, S. Pan, X. Hu, C. Miao, S. Nie, H. Mou, W. Xiao, *J. Colloid Interface Sci.* **2023**, *639*, 133.

[22] J. C. Bürger, S. Lee, A. Penn, S. Gutsch, M. Kolhep, J. Büttner, A. Fischer, F. M. Ross, M. Zacharias, *Adv. Energy Sustain. Res.* **2022**, *3*, 2200098.

[23] F. Tian, Y. Cheng, Y. Zhang, Q. Zhao, Q. Shi, Y. Zhang, C. Zhou, S. Yang, X. Song, *Mater. Lett.* **2021**, *284*, 129019.

[24] Q. Tian, Y. Chen, W. Zhang, Z. Sui, L. Yang, *J. Alloys Compd.* **2020**, *820*, 153404.

[25] Z. Wen, C. Gu, Y. Yin, M. Bayati, T. X. Liu, J. Huang, *Appl. Surf. Sci.* **2021**, *568*, 150969.

[26] F. Chen, Z. Chen, Z. Dai, S. Wang, Z. Zhang, D. Chen, *J. Alloys Compd.* **2020**, *816*, 152495.

[27] B. Zhang, J. Zhou, X. Sun, B. Luo, D. Li, X. Gu, Y. Zhao, *Adv. Mater. Technol.* **2021**, *6*, 2000849.

[28] Y. Jin, Y. Tan, X. Hu, B. Zhu, Q. Zheng, Z. Zhang, G. Zhu, Q. Yu, Z. Jin, J. Zhu, *ACS Appl. Mater. Interfaces* **2017**, *9*, 15388.

[29] R. Chen, X. Xue, Y. Hu, W. Kong, H. Lin, T. Chen, Z. Jin, *Nanoscale* **2019**, *11*, 13282.

[30] A. A. Bolzan, C. Fong, B. J. Kennedy, C. J. Howard, *Acta Crystallogr. Sect. B* **1997**, *53*, 373.

[31] A. A. Bolzan, C. Fong, B. J. Kennedy, C. J. Howard, *Acta Crystallogr. Sect. B* **1997**, *53*, 373.

[32] J. F. Mammone, M. Nicol, S. K. Sharma, *J. Phys. Chem. Solids* **1981**, *42*, 379.

[33] M. Rezaee, S. M. Mousavi Khoie, K. H. Liu, *CrystEngComm* **2011**, *13*, 5055.

[34] Y. Zou, H. Li, K. Qin, Y. Xia, L. Lin, Y. Qi, Z. Jian, W. Chen, *J. Mater. Sci.* **2020**, *55*, 5994.

[35] F. Maroni, G. Carbonari, F. Croce, R. Tossici, F. Nobili, *ChemSusChem* **2017**, *10*, 4771.

[36] A. M. Haregewoin, A. S. Wotango, B.-J. Hwang, *Energy Environ. Sci.* **2016**, *9*, 1955.

[37] M. A. Kebede, *Curr. Opin. Electrochem.* **2020**, *21*, 182.

[38] S. Zhao, C. D. Sewell, R. Liu, S. Jia, Z. Wang, Y. He, K. Yuan, H. Jin, S. Wang, X. Liu, Z. Lin, *Adv. Energy Mater.* **2020**, *10*, 1902657.

[39] E. Peled, S. Menkin, *J. Electrochem. Soc.* **2017**, *164*, A1703.

[40] R. Fong, U. von Sacken, J. R. Dahn, *J. Electrochem. Soc.* **1990**, *137*, 2009.

[41] P. Daubinger, M. Göttlinger, S. Hartmann, G. A. Giffin, *Batter. Supercaps* **2023**, *6*, 202200452.

[42] H. Moon, M. Zarrabeitia, E. Frank, O. Böse, M. Enterría, D. Saurel, I. Hasa, S. Passerini, *Batter. Supercaps* **2021**, *4*, 960.

[43] K. Pomoni, M. V. Sofianou, T. Georgakopoulos, N. Boukos, C. Trapalis, *J. Alloys Compd.* **2013**, *548*, 194.

[44] K. B. Oldham, J. C. Myland, A. M. Bond, *Electrochemical Science and Technology : Fundamentals and Applications*, John Wiley & Sons, Hoboken, NJ, **2011**.

[45] W. Weppner, R. A. Huggins, *J. Electrochem. Soc.* **1977**, *124*, 1569.

[46] R. A. Huggins, *Solid State Ionics* **1998**, *113–115*, 57.

[47] D. Qu, W. Ji, H. Qu, *Commun. Mater.* **2022**, *3*, 1.

[48] E. Barsoukov, J. R. Macdonald, *Impedance Spectrosc* **2018**.

[49] B. A. Boukamp, *Solid State Ionics* **1986**, *20*, 31.

[50] N. A. Al-Omair, S. M. Reda, F. M. Al-Hajri, *Adv. Mater. Phys. Chem.* **2014**, *4*, 29.

[51] A. S. Bakri, M. Z. Sahdan, F. Adriyanto, N. A. Raship, N. D. M. Said, S. A. Abdullah, M. S. Rahim, *InAip Conference proceeding*, **2017**, *1788*, 30030.

[52] D. Park, M. S. Lee, *RSC Adv.* **2019**, *9*, 3203.

[53] X. Jiang, Y. Wang, T. Herricks, Y. Xia, *J. Mater. Chem.* **2004**, *14*, 695.

[54] Y. Wang, X. Jiang, Y. Xia, *J. Am. Chem. Soc.* **2003**, *125*, 16176.